Dynamic studies of small animals with a four-color diffuse optical tomography imager

Christoph H. Schmitz and Harry L. Graber
NIRx Medical Technologies LLC, Glen Head, New York 11545 and Department of Pathology, SUNY Downstate Medical Center, Box 25, 450 Clarkson Avenue, Brooklyn, New York 11203

Yaling Pei
NIRx Medical Technologies LLC, Glen Head, New York 11545

Mark Farber
Department of Pathology, SUNY Downstate Medical Center, Box 25, 450 Clarkson Avenue, Brooklyn, New York 11203

Mark Stewart
Department of Physiology and Pharmacology, SUNY Downstate Medical Center, Box 31, 450 Clarkson Avenue, Brooklyn, New York 11203

Rita D. Levina
NIRx Medical Technologies LLC, Glen Head, New York 11545

Mikhail B. Levin
Department of Pathology, SUNY Downstate Medical Center, Box 25, 450 Clarkson Avenue, Brooklyn, New York 11203

Yong Xu and Randall L. Barbour[a)]
NIRx Medical Technologies LLC, Glen Head, New York 11545 and Department of Pathology, SUNY Downstate Medical Center, Box 25, 450 Clarkson Avenue, Brooklyn, New York 11203

(Received 12 May 2005; accepted 25 July 2005; published online 21 September 2005)

We present newly developed instrumentation for full-tomographic four-wavelength, continuous wave, diffuse optical tomography (DOT) imaging on small animals. A small-animal imaging stage was constructed, from materials compatible with in-magnet studies, which offers stereotaxic fixation of the animal and precise, stable probe positioning. Instrument performance, based on calibration and phantom studies, demonstrates excellent long-term signal stability. DOT measurements of the functional rat brain response to electric paw stimulation are presented, and these demonstrate high data quality and excellent sensitivity to hemodynamic changes. A general linear model analysis on individual trials is used to localize and quantify the occurrence of functional behavior associated with the different hemoglobin state responses. Statistical evaluation of outcomes of individual trials is employed to identify significant regional response variations for different stimulation sites. Image results reveal a diffuse cortical response and a strong reaction of the thalamus, both indicative of activation of pain pathways by the stimulation. In addition, a weaker lateralized functional component is observed in the brain response, suggesting presence of motor activation. An important outcome of the experiment is that it shows that reactions to individual provocations can be monitored, without having to resort to signal averaging. Thus the described technology may be useful for studies of long-term trends in hemodynamic response, as would occur, for example, in behavioral studies involving freely moving animals. © *2005 American Institute of Physics.*
[DOI: 10.1063/1.2038467]

I. INTRODUCTION

An increasing variety of imaging techniques has become available in recent years for the noninvasive study of experimental animals, especially small rodents such as rats and mice. An appeal of noninvasive imaging, compared with the traditional histological approach, is the possibility of conducting longitudinal studies on the same animals, thereby greatly reducing the number of required sacrifices, which is desirable on both ethical and economic grounds. Other advantages are the improved information value obtained by following the same individual, and generally higher throughput. There is considerable interest in pharmaceutical applications of small animal imaging, such as investigating the effect of drugs on the progression of diseases (e.g., cancer, atherosclerosis, or Alzheimer's in transgenic models) or on acute pathological events such as tissue infarction. In addition, animal imaging is employed in a wide spectrum of

[a)]Author to whom correspondence should be addressed; electronic mail: randall.barbour@downstate.edu

medical and biological fields, such as developmental studies, transplantation research, and experimental neurology, among others.

Available animal imaging modalities include high-resolution structural techniques, such as x-ray computed tomography (CT), magnetic resonance imaging (MRI), and ultrasound imaging, and modalities suitable for functional studies such as positron emission tomography, single photon emission CT, and functional MRI. Because the assessment of tissue function ultimately is linked to the detection of specific marker molecules—either intrinsic or extrinsic—this latter class of methods also has come to be known as molecular imaging.[1]

In addition to these "traditional" methods, a variety of optical techniques for imaging experimental animals has attracted increased intention. The appeal of optical methods is in their inherent sensitivity, the existence of intrinsic and exogenous contrast agents exhibiting absorption or fluorescence over a wide optical spectrum, high temporal resolution ("real-time imaging") and an instrumentation effort that is more economical, safe, and manageable than those for other modalities. In addition, some of the basic limitations associated with optical imaging of human subjects (i.e., limited tissue penetration and a strongly depth-dependent spatial resolution) are greatly reduced in small animal imaging applications, because of the smaller target sizes encountered. Commercial planar optical fluorescence and bioluminescence imagers are now available, e.g., from Xenogen, Hamamatsu, GE, Siemens, and others. In addition, the development of tomographic fluorescence imaging of small animals is currently being pursued by a number of groups.[2,3]

Yet another area of investigation involving small animals is the use of near-infrared absorption imaging to explore functional activation and tissue-vascular coupling in the brain. The appeal of near infrared spectroscopy is the ability to measure local concentrations of the different forms of hemoglobin, i.e., oxyhemoglobin (Hb_{oxy}) and deoxyhemoglobin (Hb_{red}). The sum of these yields an estimate of the total hemoglobin (Hb_{tot}) concentration, or blood volume, in tissue. As early as the mid 1980s, two-dimensional detector arrays were used to image the illuminated exposed brain of experimental animals.[4] This technique, applied by a number of groups,[5–7] has the advantage of a relatively straightforward instrumental implementation as well as high temporal and spatial resolution. A general limitation of the method, however, is the restriction to imaging superficial phenomena. Another disadvantage is the requirement for surgery to thin the skull or to expose a portion of the animal's brain.

In contrast to direct planar imaging, diffuse optical tomography (DOT) employs arrays of multiple illumination and detection sites, and utilizes numerical image reconstruction algorithms to obtain images of subsurface phenomena. This capability allows for noninvasive transcranial studies of brain function.

A variety of instrumental and numerical approaches have been introduced by different groups over the last decade for DOT imaging of animals. Continuous wave (cw) DOT studies of rat brain activity have been reported that employ up to nine sources and 16 detectors in reflection-type geometries in which the optical probes are arranged on the dorsal aspect of the head (i.e., cranium).[8–11] In addition, frequency domain studies of rat brain activity have been performed using an eight-detector, eight-source ring geometry.[12]

In this report, a newly developed imager for CW-DOT studies on small animals is presented. The instrument is based on the dynamic near-infrared optical tomography (DYNOT) system (NIRx Medical Technologies), which so far has been used for clinical imaging studies of the breast, limb, and brain.[13–15] The system has been expanded to achieve four-wavelength operation, and an imaging stage that allows fixation of the animal and stable probe positioning has been developed. Instrument performance and stability have been evaluated using laboratory phantoms and in a rodent animal model. The latter studies reveal strong activation in the thalamic region, demonstrating the ability to image the entire brain volume. Another, equally important outcome of the experiment is that it shows that reactions to individual provocations can be monitored using the described instrument, without having to resort to signal averaging to increase the signal-to-noise ratio (SNR). This raises the possibility of conducting DOT behavioral studies, that is, of monitoring long-term trends in vascular dynamics, such as would occur in freely moving, nonanesthetized animals.

II. INSTRUMENTATION

The instrument provides multiplexed illumination of tissue at up to 32 locations (source positions), at a rate of about 60–90 source (S) positions per second depending on operating conditions. A fast optical switch (OS) sequentially directs the combined output from laser diodes of different wavelengths into optical fibers that are used for tissue illumination. Lasers are intensity-modulated at distinct frequencies in the range of 4–11 kHz, and lock-in detection is used to separate the optical signals originating from different lasers. Light emerging from a target site of interest is collected and transmitted via optical fiber bundles to one of up to 32 available detector (D) channels. The instrument operates all detector channels simultaneously, to maximize data acquisition rates. Source multiplexing, while reducing the acquisition speed, allows for dynamic measurement ranges that are unobtainable with frequency-encoded parallel-illumination schemes (recently, an alternative wavelength-multiplexed parallel-illumination scheme has been described,[16] which does not suffer from this latter restriction, but does at present require costly instrumentation). Our instrument achieves a large dynamic range (approximately $1-10^9$) through the electronic adjustment of the sensitivity setting of each detector channel in synchrony with the moving illumination site. Here, the dynamic range of a detector is defined as the ratio of its saturation limit at the lowest gain setting to its electronic noise floor at the highest gain setting. The latter is on the order of 1 pA_{rms}, in a 144 Hz detection bandwidth, for the given frequency range (i.e., 5–11 kHz). We recognize, however, that measured signals have to lie well above this limit to achieve a SNR sufficient for meaningful data interpretation. Details of the electronic gain switching scheme can be found in Refs. 17 and 18. The large dynamic range of

the instrument allows for implementation of complete, or nearly complete, tomographic measurements, rather than restricting the user to less informative transmission-only or reflection-only *S-D* configurations. The imager is operated through a graphical user interface (GUI) implemented in the LABVIEW™ (National Instruments, Austin, TX) language, which provides measurement setup and data display as well as a host of checking procedures assessing adequacy of the measurement setup, data integrity, and instrument performance. Detailed descriptions of these capabilities also have appeared previously.[19]

In addition to the imaging hardware, the measurement system comprises a variety of integrated software solutions for instrument control and testing, image reconstruction, data analysis, and data display. These functions have been described previously,[13] so that only details germane to the presented results are reviewed here.

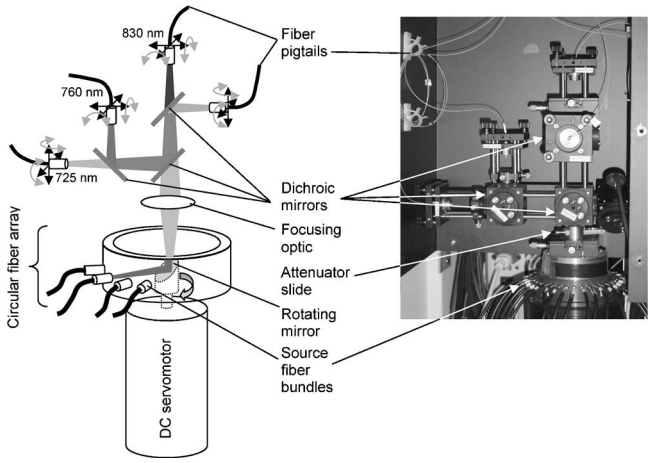

FIG. 1. Optical switch and four-wavelength mixing optic developed for the small-animal imager: (left) schematic drawing of the assembly; (right) photograph of device.

A. Four-wavelength capability

DOT measurements performed at more than one wavelength yield spectroscopic information that can be used to separate contributions to the optical signal stemming from different tissue components. Most commonly, two wavelengths in the near-infrared region, between approximately 670 and 850 nm, are used to differentiate between Hb_{oxy} and Hb_{red} concentrations. This is done under the assumption that absorption from other prominent chromophores (e.g., water, lipids, myoglobin, cytochromes) in that range is weak and/or slowly varying over time, and can be neglected. The Hb_{tot} content can then be estimated as the algebraic sum of the measured concentrations of the two hemoglobin oxygenation states. More wavelengths allow the quantification of additional tissue compounds or extrinsic contrast agents. Recently, investigators have increasingly explored the benefit of adopting more than two wavelengths to increase the information content of DOT measurements to improve diagnostic specificity and sensitivity.[20–22]

Even though the DYNOT instrument was designed for four-wavelength capability, until now it has been used exclusively for two-wavelength measurements. In the following, the instrumentation features particular to the four-color version of the imager are described.

The four-color instrument uses a commercial modular laser controller (Model 8000, Newport, Irvine, CA) equipped with four laser driver modules (Model 8630, Newport, Irvine, CA) to allow simultaneous operation of four thermoelectrically cooled laser diodes. Each module is programmed to sinusoidally modulate the intensity of its laser output, at a unique frequency; care has been taken to avoid overlap of the modulation frequencies' harmonics to eliminate interwavelength crosstalk. The laser diodes (High Power Devices, Brunswick, NJ) with fiber pigtails and gradient index rod lens output collimators operate at nominal wavelengths of 726, 760, 810, and 830 nm. The output power of each laser is set to an average value of approximately 100 mW, resulting in a total average source illumination intensity of approximately 100 mW (25 mW/source). This power level provides for maximal laser stability but is much greater than needed for optical studies; accordingly, a neutral density filter is placed in the optical path to attenuate the optical power delivered to the tissue surface to approximately 10 mW. The "butterfly"-style laser packages are mounted in telecom sockets (Model 744, Newport, Irvine, CA), which are provided with forced-air cooling to improve cooling efficiency and temperature stability.

A four-wavelength mixing optic was developed to collinearly overlay the laser beams and to focus them into the optical switch. A photograph of the optic and a schematic representation of the wavelength mixing process are presented in Fig. 1. The wavelength multiplexer uses dichroic mirrors (DMs) (Omega Optical, Brattleboro, VT) to combine the beams by wavelength-selective transmission and reflection. A set of three optics is used to make the four beams colinear. The two shorter-wavelength pairs (726 and 760 nm) and the two longer-wavelength pairs (810 and 830 nm) are each combined by one DM. The two resulting beams are then combined by a third DM. Each of these steps has greater than 85% efficiency for all beams. Every laser collimator permits individual adjustment of lateral translation and tilt angle, to facilitate collinearization of the beams. All DMs are mounted to allow positional adjustment in five degrees of freedom (three rotational and two linear). The optomechanical components used in the device were obtained from Thorlabs (Newton, NJ), or were custom fabricated. Neutral density filters of different optical densities can be inserted into the combined beam by means of a custom-built sliding mechanism, to adjust illumination intensity. The current system offers unattenuated illumination as well as attenuation of intensity by factors of 10 and 100. The optical switch for the new imager is identical to the design used in the dual-wavelength systems.[17]

The animal imager employs a programmable multichannel optical detector (PMOD) housing up to 32 individual detector channels, which has been described in detail before.[17] In the two-wavelength version, each detector channel is equipped with a modular lock-in circuit, which serves to separate the signals of two lasers. Each channel can accept a second lock-in circuit in the form of a plug-in module, to provide four-wavelength demodulation. Conversion of the PMOD from two- to four-wavelength operation was

achieved by installing these modules and by inserting a second digital phase shifter card, which provides a reference signal to the added lock-in circuits.

The instrument uses two data acquisition (DAQ) boards, each capable of digitizing up to 64 channels, to acquire the up to 128 output signals (32 detector channels $\times 4$ wavelengths) generated by the PMOD. These LABVIEW-programmable devices (PCI-6033E, National Instruments, Austin, TX) are housed in the peripheral computer interconnect bus of a personal computer.

The DYNOT control GUI was modified to interrogate the two DAQ boards and to provide instrument setup functions as well as data display and storage for four wavelengths. Likewise, a series of automated data quality checks recently introduced into the DYNOT software[13] was adapted to four-color operation. The GUI functionality has been further expanded by addition of a LABVIEW implementation of a previously described calibration algorithm[18] that estimates relative variations in source strengths and source and detector coupling efficiencies based on phantom measurements. The algorithm is described, and calibration results for the four-wavelength imager are presented, in Sec. II C.

B. MRI compatible small animal imaging platform

A challenge common to all DOT applications is the creation of a probe-tissue interface that is flexible enough to adapt to the specific size and anatomy of the target under investigation, yet rigid enough to ensure stable and efficient optical contact. Figure 2 shows an interfacing device developed for optical probe placement on small animals under stereotaxic fixation. The configuration used for optical studies of the rat brain is shown, although the device can be adapted to imaging other sites of the animal. The rat is stabilized in a prone position by an adjustable cradle, and its head is fixed via two ear bars and one bite bar. The majority of probes are positioned over the dorsal aspect of the head by a cantilevered holder, which is adjustable in height and pitch. The probe holder is formed by a plate with 48 holes, each of which acts as a fiber receptacle, arranged in a 6×8 rectangular grid [see Figs. 2(b) and 3]. The center-center distance between neighboring holes is 3.15 mm along both grid axes. To provide a friction grip on the fiber ends, the probe holder plate has a layered structure, with a foam rubber pad sandwiched between two rigid plates. The compression of the rubber can be adjusted, thereby controlling the frictional hold of fibers in their holes. This design allows rapid yet stable placement of fibers in a variety of arrangements and with high density; the distance between fiber tips is about 0.7 mm. Lateral fiber receptacle holes are increasingly tilted in the coronal plane to account for anatomical curvature of the animal's skull (see Fig. 3).

A grid-like probe arrangement on the dorsal head restricts the measurement to a purely reflection-type geometry. To enhance the information content of the animal-brain measurements, opposing probe locations were introduced that add transmission measurements to the tomographic data set. Therefore the imaging platform provides for positioning of

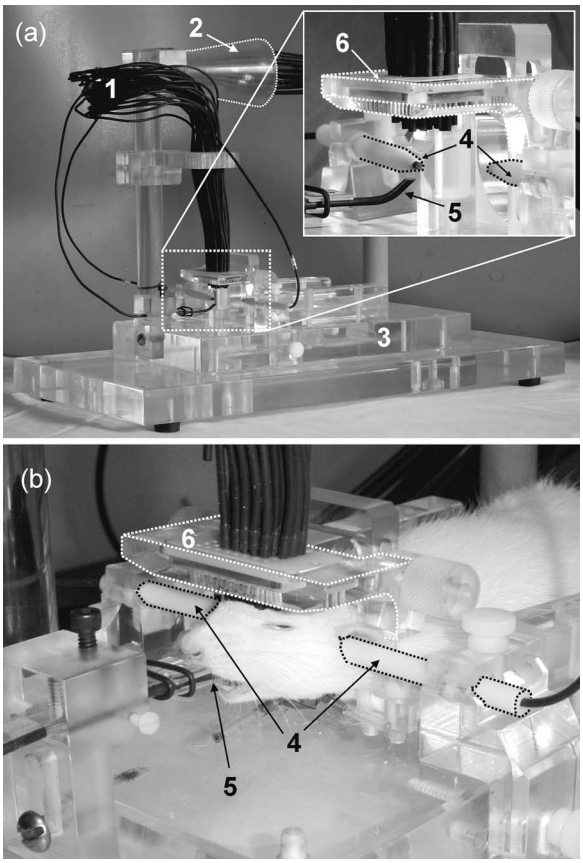

FIG. 2. Photographs of small-animal imaging platform. (a) Platform with fiber optics (1), strain relief (2), and animal cradle (3); inset shows ear bars with probes (4), curved mouth fiber (5), and dorsal rectilinear optode array (6). (b) Animal fixation and probe placement in the experiment.

one probe in each ear, and up to two probes inside the mouth of the animal, in addition to the fibers located on top of its head. The ear probes, which are identical to the dorsal probes, are introduced through an axial bore in each ear fixation bar. Fibers used inside the mouth have curved end ferrules and slanted tips to allow good optical contact with the roof of the mouth of the animal [see Fig. 3(b)]. The mouth probes are attached to the bite bar, which fixes the animal's incisors.

The imaging platform has a fiber strain relief to protect the fiber optics against mechanical damage, and to decouple the probe-tissue interface from movements of the optical cables.

The small-animal platform was constructed entirely from nonmagnetic materials, so that it would not interfere with MRI studies if used in a magnet. The device shown in Fig. 2 is a proof-of-design implementation that is not intended for in-magnet use, and therefore does not reflect any specific measures to accommodate the space constraints of a magnet bore. Adapting the device to in-magnet studies is straightforward because its most critical design elements (i.e., fiber holders) already conform to the typical dimensional requirements. The only change required on the part of the probe holders would be reduction of the length of the ear bars and a miniaturization of some of the adjustment and support elements. The most significant design changes required would be replacement of the current base plate with a narrow plat-

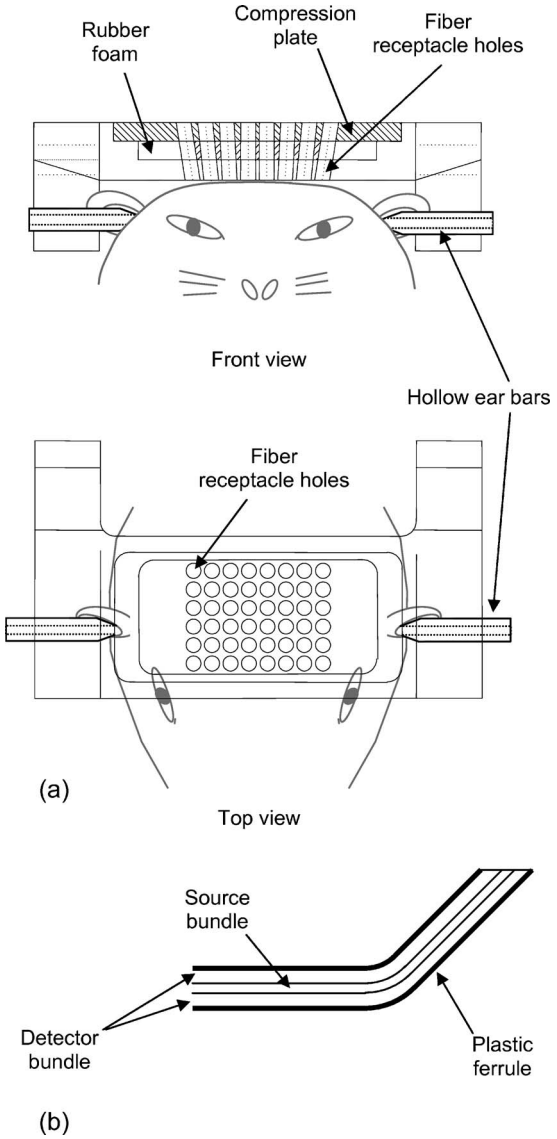

FIG. 3. (a) Schematic of the adjustable fiber array holder and its position on the animal's head and (b) cross-sectional schematic of the bent mouth probe.

form and replacement of the vertical fiber strain relief post by a low-profile implementation. All of these modifications are straightforward and do not impact on the proven functionality of the device.

Each of the fiber optic cables used in the animal imager acts as both a source and a detector, by combining illumination and detection fibers in a bull's-eye arrangement at the probe end, similar to designs that have been described before.[18] Whereas the fiber probes for human applications have diameters of about 3.5 mm to maximize light collection efficiency, the animal imager uses smaller-diameter fibers to achieve high probe placement density on small targets. The source and detector branches have optical aperture diameters of 0.8 and 2.0 mm, respectively, and the probe end has an outer diameter of 2.4 mm. Because of the relatively weak optical attenuation encountered, these probes still have sufficient light collection efficiency to allow full tomographic imaging on small animals. The fiber optics use plastic ferrules at the probing end to allow their use in in-magnet studies. The cables, which have nonmagnetic sheathing, are 4.6 m long so the instrument can be operated at a safe distance from a magnet.

C. Instrument performance

Before the imager was used for physiological studies, its performance with regard to signal noise and stability was carefully assessed. In addition, a four-wavelength implementation of a previously described algorithm was used to achieve calibration of relative optical probe coupling efficiencies to establish optical coupling reproducibility.

1. Signal stability

The achievable signal quality of the imager is determined by two principal sources of noise. One is the occurrence of electronic fluctuations in the detection circuit, and the other is the presence of random variations in illumination intensity. The former is the dominating factor at higher gain settings and ultimately limits the light sensitivity of the instrument. Using an automated dark noise test, we ensured that all detector channels worked according to established noise specifications at all gain settings. The long-term drift of the detection electronics was on the order of 1 mV, or less than 1% of typical signal levels, over 1 h.

In the regime of low detector noise (i.e., at low gain settings), the achievable signal quality is limited by variations in illumination strength, which is the combined effect of variability in laser intensity and of imperfect incoupling repeatability of the OS. Despite active temperature control, lasers can show residual power fluctuations on the order of 1% on a time scale of seconds to minutes. Therefore the laser intensity is measured with a separate reference detector, for subsequent correction of data fluctuations caused by source instabilities.

The OS causes frame-to-frame variations in illumination strength due to repeatability limits of the mechanical beam-steering mechanism. This source of noise is minimized by careful optical alignment of the wavelength mixer, and by optimizing the motion protocol of the dc servo motor. Because of the motor's warming up during operation, one also needs to be attentive to long-term illumination instabilities caused by thermal drifts of optomechanical components. To determine the illumination noise for each source, readings of colocated S/D pairs (i.e., S_m/D_m), obtained with a homogeneous phantom as the target medium, were recorded. These channels are guaranteed to obtain very low gain settings, and illumination instability is by far the primary contributing factor to their overall measurement noise.

Figure 4(a) illustrates the results of a long-term stability study. Shown is the mean coefficient of variation (CV) (in %), averaged across all channels, for all four wavelengths during a continuous 3 h measurement. The standard deviation (SD) of the CV values across channels, as well as the smallest and the largest CVs, also are indicated. It can be seen that at all wavelengths, the average SNR—as defined by the CV—is larger than 100 (i.e., CV smaller than 1%). The majority of channels show CVs that are well below that mark, although some CV values greater than 1% are seen for the 726 nm source. The results demonstrate excellent long-

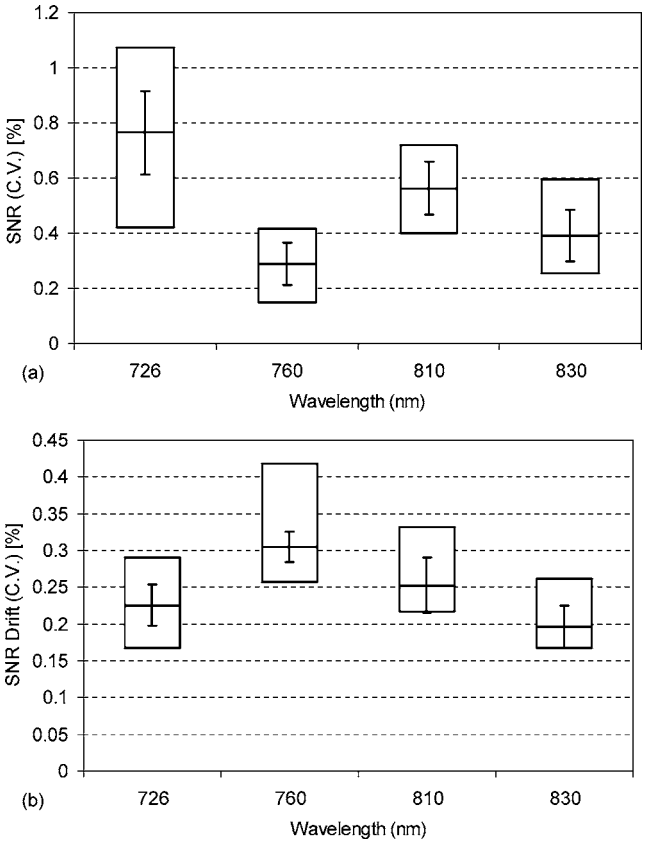

FIG. 4. (a) Long-term stability of the optical signal. Shown for each wavelength are the mean, the minimum, and the maximum CV of the signal variations for all channels during 3 h of continuous instrument operation. Error bars indicate standard deviation. (b) Long-term drift of the noise in the optical signal. Shown for each wavelength are the mean, the minimum, the maximum, and the standard deviation (error bars) of temporal fluctuations in signal CV for all channels during 3 h of instrument operation.

term signal stability over a period encompassing approximately 8×10^5 mechanical source movements.

Also shown, in Fig. 4(b), are the long-term changes in SNR. Plotted for each wavelength is the mean CV value, averaged over all channels, of changes in SNR over the course of the 3 h scan. Long-term SNR variations were obtained by calculating the signal CV over 100 consecutive time points, at 5000 time-frame intervals throughout the measurement, and then computing the mean and SD of the resulting values. Also indicated are the SD (error bars) across channels and the smallest and the largest SNR variations. The results shown demonstrate that over the course of 3 h the signal noise varies by less than 0.5% for all channels, indicating excellent long-term stability of the achieved SNR.

2. Calibration study

We have previously presented a calibration protocol,[18] which estimates relative variations among the illumination strengths of the source channels (expressed as a source strength factor s_i, with $0\leqslant s_i\leqslant 1$) and relative sensitivity discrepancies among the detector channels (expressed as a detector sensitivity factor d_j, with $0\leqslant d_j\leqslant 1$). Interchannel variations in illumination intensity are the result of varying incoupling and transmission efficiencies of individual source fiber optics. Differences in detection sensitivity are present because of varying fiber transmission, fiber-detector alignment, and electronic component tolerances for individual detector channels.

The calibration procedure serves two purposes. First, knowledge of the s_i and d_j values allows correction of the measured data, thus enabling comparison of readings from different channels. While this knowledge is not required for the reconstruction of dynamic target features,[23,24] it adds information necessary to establish the optical properties of the static background of the medium. The second function is that the calibration protocol provides objective measures of hardware integrity and instrument performance. For example, tracking changes in the s_i and d_j values allows the operator to pinpoint source or detector channels showing deteriorating performance, such as may be caused by damaged fibers, contaminated probe tips, or degraded detection electronics.

The calibration method is based on measurements on a phantom, whose shape and optical property distribution are rotationally invariant with respect to the probe geometry. In this case the transmitted light intensity for all S/D combinations depends only on the S-D separation. Therefore, deviations in the readings for different probing pairs having the same S-D distance can be attributed to differences in source strength and/or to variations in detector channel sensitivity. Formally, the influence of the target properties and the instrumental factors on the measured signals can be expressed by the matrix equation $\mathbf{R}=\mathbf{SMD}$, where $\mathbf{R}$ contains the measured readings from all S-D combinations, $\mathbf{M}$ represents the fraction of light transmitted from S_i to D_j by the medium, and $\mathbf{S}$ and $\mathbf{D}$ are diagonal matrices containing the source strength coefficients and detector sensitivity factors, respectively. The animal imager was calibrated using a cylindrical phantom vessel (white Delrin™, 76.2 mm o.d., 3 mm wall thickness) filled with diluted Intralipid™ (IL). The probes were placed equidistantly on the vessel surface in a plane perpendicular to the cylinder's main axis. To achieve factorization of the acquired readings according to the above matrix equation, we used a published algorithm that makes use of prior knowledge of the form of $\mathbf{M}$ for a cylindrical problem geometry.[18]

When performing calibration for the purpose of assessing instrument performance, it is legitimate to use a medium and geometry different from those actually used in physiologic experiments. Here we opted to use a circular geometry because the appropriate algorithm was readily available, and the solid cylindrical laboratory phantom offers proven stability, both experimentally and numerically. However, to establish coupling coefficients for use in image reconstruction, it would be desirable to calibrate the instrument using the actual probe holder with a phantom whose consistency and external geometry resemble those of the target. This would achieve the best approximation to the actual measurement conditions and minimize the chance of altering calibration factors while switching fiber optic probes from one measuring head to another. It should be noted that the existing calibration algorithm for cylindrical phantoms can be generalized to more complex geometries, such as that encountered in the rat imaging platform.

Figure 5 summarizes the results of four calibration stud-

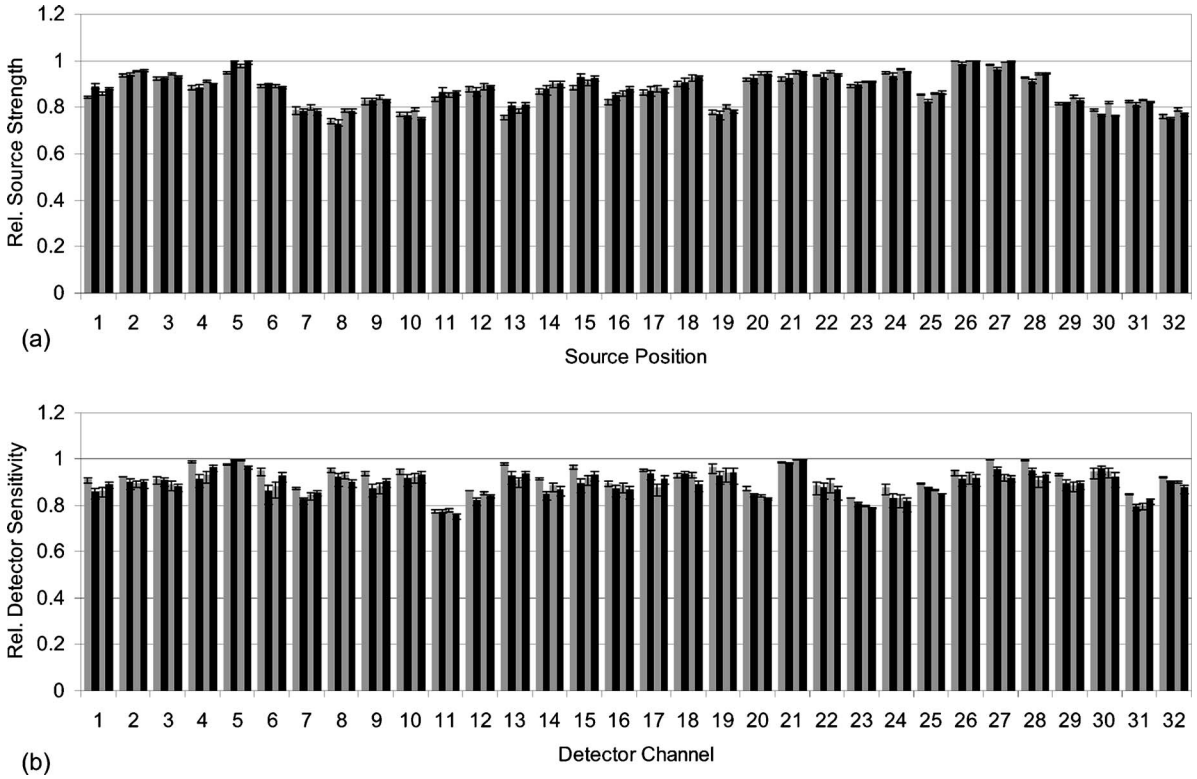

FIG. 5. Four-wavelength calibration results for four measurements performed over 2 days: (a) mean source coupling coefficients s_i and (b) mean detector sensitivity coefficients d_i. Error bars indicate extreme values. Viewing from left to right within each group of bars, the data are arranged in the order 726, 760, 810, and 830 nm.

ies performed over the course of two days. Panel 5(a) depicts the results of the source calibration. Each bar represents the average of the s_i values obtained from four calibration studies, and the error bars indicate the minimum and the maximum value found for each channel. The first three measurements were performed with an IL concentration of 0.5%, and 1% IL was used in the last experiment. The source calibration factors are normalized with respect to the highest occurring value, which is assigned a value of unity. The bars are plotted in groups of four, corresponding to the results for four different wavelengths. It can be seen that within each group of four, the s_i values are closely matched (CV less than 5%), indicating similar fiber incoupling and transmission efficiencies for all wavelengths. More significant, the repeatibilities within all channels are very similar (CV$\pm$1%). This is indicative of excellent opto-mechanical stability on the part of the instrument, and of high reproducibility of the calibration procedure. The fact that there is no significant systematic difference between the results from the first three measurements and the fourth clearly demonstrates the method's independence of the optical properties of the target.

Figure 5(b) depicts the detector calibration results. The d_j values are plotted in groups of four, each bar of the group corresponding to a different wavelength. Each bar represents the mean result from four calibrations, and error bars indicate the smallest and largest value obtained for each channel. While not as homogeneous as the source factors, the d_j results for different wavelengths in each channel are similar (within 10%). The variation of d_j values across experiments is small—within 2% for most channels—demonstrating excellent reproducibility. The somewhat larger variability of the detector calibration values, compared to the source results, is explained by the fact that source-target coupling is much more robust against changes in alignment and interface condition than is target-detector coupling. For example, slight positional or angular changes of the source fiber typically will not have a strong impact on the fraction of light entering the target. For the detector fiber, however, such a change may significantly alter the boundary conditions under which diffuse light enters the fiber, impacting on the measured amount of light.

III. IMAGING RAT BRAIN HEMODYNAMICS

To test the optical imager's performance in small animal studies, a well-understood paradigm that uses electric paw stimulation to evoke somatosensory responses was adopted. The primary goal of the experimental study was to demonstrate the instrument's capability of sensing hemodynamic changes in the rat brain with high sensitivity in a full-tomographic probing geometry. As shown below, the observed SNR was sufficiently high to permit data analysis on individual epochs, thus circumventing the need for averaging over trials. Consequently, statistical evaluations of hemodynamic responses between trials on the same paw, as well as between results for different stimulation sites, were obtainable.

We chose to electrically stimulate the animal's four limbs for three related reasons. First, electrical stimulation gives the most precise control of the timing of neural circuit activation and any related hemodynamic changes, and we are particularly interested in the temporal evolution of hemody-

namic changes that occur in relation to neural activity. Second, the level of neural activity can be controlled to some degree by varying the stimulus intensity as well as the frequency of the current pulses and the total duration of the stimulus train. Finally, by activating brain regions that are distinct (i.e., by stimulating each paw in succession), we introduced a spatial separation of activity that will be important for interpretation of both the spatial resolution achievable with the instrument and the temporal evolution of hemodynamic changes associated with neural activation.

A. Experimental methods

1. Data analysis and image reconstruction

All data processing and image reconstruction was performed with the dynaLYZE software package (NIRx, Glen Head, NY), which is based on the MATLAB™ computing language (The MathWorks, Inc., Natick, MA).[25]

Raw data were first subjected to a preprocessing procedure that serves to condition signals for analysis and image reconstruction. In the first step, the CV during the baseline period was calculated for all channels, and those having CVs greater than 15% were excluded from further processing. This threshold level represents a value approximately twice the variability in signal level seen due to naturally occurring vascular rhythms. In the study whose results are presented here, 954 out of 961 channels (>99%) were accepted for analysis, demonstrating the good signal quality achievable for virtually all *S-D* combinations. The time-varying signals for the channels that were not excluded in the preceding step were then corrected for variations in laser power, which was continuously recorded during the experiment. Thereafter, data were normalized to the time-averaged mean of the initial baseline period for use in the image reconstruction process. In the final step, estimated changes in Hb_{oxy}, Hb_{red}, and Hb_{tot} were computed for each data channel, by applying a modified Beer-Lambert (MBL) analysis as outlined in Ref. 13.

Image time series were reconstructed using a normalized-difference method (NDM) as described previously.[23] The weight matrix (Jacobian operator) for the problem was generated using a finite element method (FEM)-based algorithm to numerically solve the diffusion equation, using the forward-problem mesh shown in Fig. 6. The mesh, which presents an accurate rendering of the rat head anatomy, was developed by A. Y. Bluestone in the laboratory of A. H. Hielscher at Columbia University, NY, using high-resolution anatomic maps obtained from rat head cryosections.[9] It was kindly made available for our optical rat brain studies, and has been slightly modified to accommodate our specific fiber geometry and the size of the animal used. The modifications included moving some FEM nodes on the model boundary so they coincide with the exact fiber positions used in the experiments. In addition, the mesh was rescaled, using individual factors for each spatial dimension to match the size and shape of the head of the animal imaged. The model provides seven anatomical compartments,

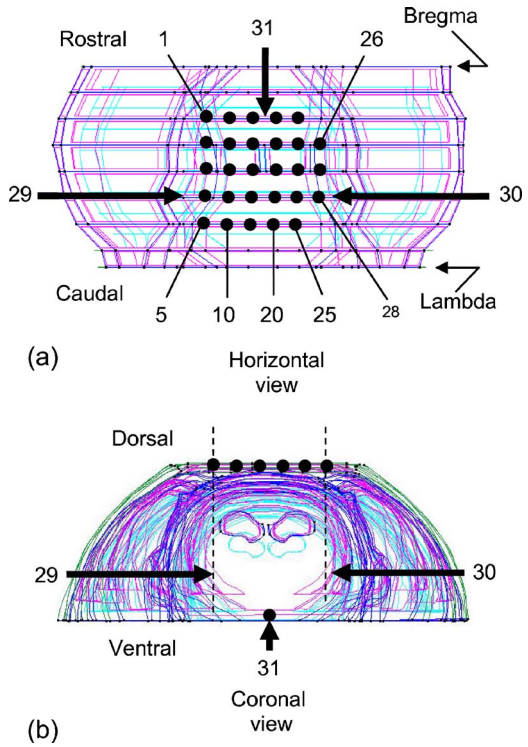

FIG. 6. Geometry used for modeling light transport in the rat head. Positions of the fiber probes are indicated: (a) horizontal (bottom) view and (b) coronal (front) view.

to which distinct sets of optical properties can be assigned: the skin layer, the skull, left and right jaw muscles, the brain, and left and right hippocampus.

A truncated singular value decomposition method was used to solve the linear perturbation equation.[24] In each node of the reconstructed absorption coefficient images for four wavelengths, time series for Hb_{oxy} and Hb_{red} concentration changes were computed by solving an algebraic system of four equations in two unknowns.[26] Hb_{tot} changes were estimated as the algebraic sum of the Hb_{oxy} and Hb_{red} time series.

A general linear model (GLM) algorithm[27] was used to calculate the best-fitting linear combination of pre-selected model functions to the different time-varying Hb signals, at each image node. The set of model functions used included one constant (offset) term, one linear and one parabolic trend term, and a function describing the idealized hemodynamic response to neuroactivation for the specific Hb state. For each of these, the analysis yields a spatial map of the GLM coefficients, indicating the magnitude of the model function at each position within an image time series. In addition, the algorithm generates confidence maps showing the statistical significance of the preceding GLM parameters, and a spatial map of the percentage of temporal variance accounted for, in each image pixel, by the idealized hemodynamic response function.

2. Animal preparation and experimental protocol

A male Sprague-Dawley rat, weighing 300–400 g, was anesthetized with urethane (1.5 g/kg i.p.) and placed in the stereotaxic imaging platform. A total of 31 fiber optic probes were placed about the animal's head; 28 of these were ar-

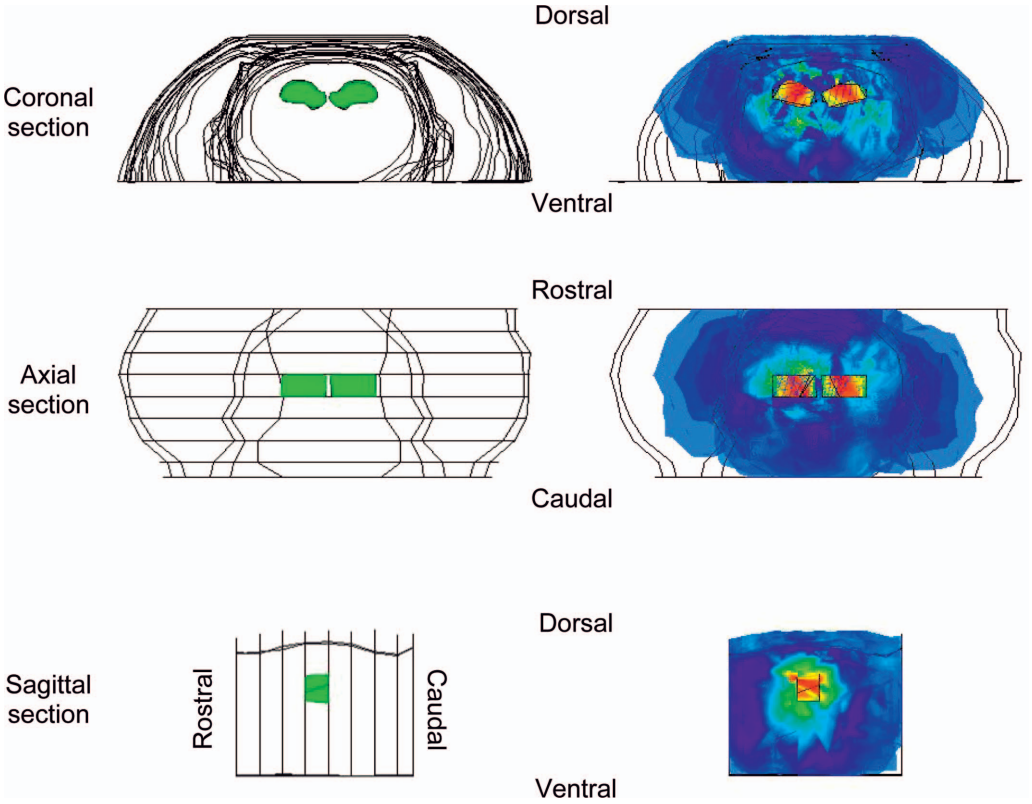

FIG. 7. (Color) Results of numerical simulation study: (left) three orthogonal views of geometrical rat head model, with region containing elevated absorption shown in green and (right) corresponding views of recovered μ_a image.

ranged in a rectilinear grid on the dorsal head, two were inserted in the ears, and one probe was located inside the mouth (see Sec. II B). The last had a curved fiber tip as described above, and care was taken that its optical surface made even contact with the roof of the mouth. The fiber arrangement on the head corresponded to the positions indicated on the FEM mesh shown in Fig. 6. The anterior and posterior boundaries are the sites of the bregma and lambda skull sutures, respectively. Care was taken to position the fibers between these suture lines and symmetrically about the midline.

After placing the animal in the imaging platform, the gain settings were determined by an automated setup procedure implemented in the imager GUI.[19] Appropriateness of gains and adequacy of fiber contact were confirmed using checkout procedures offered by the GUI[13] before initiating the measurement. A baseline period of 1300 frames ($\sim$10 min) was acquired prior to electric sensorimotor stimulation. A commercial stimulator (A-M Systems, Carlsborg, WA) was used to administer 5 mA direct current pulses (0.5 ms duration at 10 Hz repetition rate) to each paw through a low impedance stainless steel needle electrode ($<$100 kΩ, Grass Instruments, West Warwick, RI). Pulse trains lasted 3 s ($\sim$six imaging frames), and were separated by 150 imaging frames ($\sim$79 s).

B. Results

1. Numerical simulation results

Before proceeding with experimental studies, numerical simulations were conducted to evaluate the image quality achievable with the available measurement geometry and image reconstruction method. Using a FEM solver and the diffusion approximation, reference detector readings were computed for the probe positions indicated in Fig. 6, under an assumption of an optically homogeneous target with $\mu_a = 0.006\ \text{mm}^{-1}$ and $\mu_s = 1\ \text{mm}^{-1}$. A second set of readings, representing the measured response to a perturbation, was calculated using identical background optical properties and a threefold absorption increase in the hippocampal area (i.e., $\mu_a = 0.018\ \text{mm}^{-1}$). The relative differences between these data sets were used in the NDM-based image reconstruction outlined above. Care was taken to use different meshes for the forward and the reconstruction calculations in order to avoid an "inverse crime." For that purpose a second mesh was generated, that has a geometry nearly identical to the one described in Sec. III A 1, but with a distinct node distribution.

Figure 7 shows the location of the perturbation within the head model, together with the reconstructed image, in three volume-rendered orthogonal views. The results reveal excellent fidelity in the recovery, of both the location and the spatial extent (approximately 6.0 mm $\times$ 4.0 mm $\times$ 3.0 mm) of the perturbation.

2. Imaging the hemodynamic response of the rat brain to paw stimulation

Spatially averaged time response of Hb signals. Figure 8 shows the time course of spatially averaged Hb signals from three successive left front paw stimulation epochs. The onset and cessation of each epoch are indicated. The curves were obtained by estimating concentration changes of the Hb

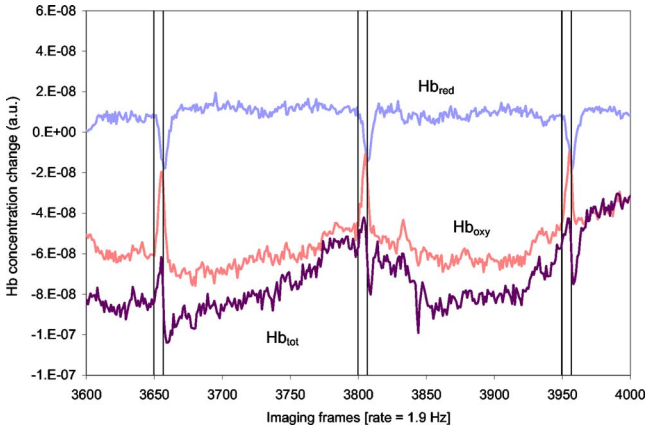

FIG. 8. Time series of the spatially integrated Hb response to stimulation. Vertical lines indicate start and cessation, for three consecutive epochs of left front paw stimulation.

oxygenation states for every *S-D* pair using the MBL method, and then averaging the results across all channels at each time point. The curves reflect the integrated response of the probed volume to stimulation. In agreement with other reports,[28–30] we observe an increase in Hb_{oxy} and a decrease in Hb_{red} concentration in response to the stimulus. A time delay also is observed between the Hb_{oxy} and Hb_{red} curves; the onset of the Hb_{oxy} response consistently occurs about one time point ($\sim$0.5 s) earlier than that of the Hb_{red} reaction. Likewise, the Hb_{oxy} signal peaks one frame ($\sim$0.5 s) before the Hb_{red} curve does. Similar delays have been shown in reports on optical studies of whisker barrel stimulation in rats.[29,30] The shape of the Hb_{tot} signal in Fig. 8 shows a biphasic behavior, which is not in agreement with the monophasic increase in Hb_{tot} attributed to enhanced local cerebral blood flow following neuroactivation as reported in Refs. 28–30. Analysis of the reconstructed image time series, as carried out in detail in Sec. III B 2 "GLM analysis of image time series" below, reveals occurrences of both the expected (i.e., Hb_{tot} increase) response to stimulation as well as an inverted response, in different areas of the head. The volume-integrated signal in Fig. 8 therefore shows a mixture of these responses, leading to increased complexity in its functional shape.

To quantify the magnitude of overall tissue reaction to the stimulus, and to assess the precision of our measurements, variations in global reactivity strength between individual stimulation epochs were derived, by spatially averaging the reconstructed images and calculating the areas enveloped by the individual peaks in the resulting time series. Table I shows, for each Hb state, the magnitude (i.e., absolute areas enclosed by the curves were computed, in order to obtain positive numbers and to avoid a net area close to zero for the biphasic Hb_{tot} pulse) mean, standard deviation, and CV values obtained from six stimulation repetitions on each forepaw. For both paws, reaction of the Hb_{oxy} signal to the provocation is significantly stronger than those of the other Hb states. Analysis indicates that the differences $Hb_{oxy}-Hb_{red}$ and $Hb_{oxy}-Hb_{tot}$ both are highly significant ($p<10^{-5}$). Comparing left versus right response strengths, we found no significant difference between the Hb_{oxy} signals ($p=0.26$), but a differentiation is observed for Hb_{red} ($p=0.05$), and Hb_{tot} ($p=0.03$) signals. The mean values are, however, systematically higher for the left paw in all cases, supporting the perception of an overall stronger response for this stimulation side. This finding may be explained by variation of experimental factors, such as placement of the stimulating electrode or effects of anesthesia; it may also, however, suggest biological preference (handedness) of the animal. The CV data allow us to make a statement about the precision of our experiment; the spatially integrated tissue reactivity varies within about 20% for most cases except for the Hb_{oxy} signals, where the precision is on the order of 30%.

TABLE I. Response strength variation.

Side	Hb state	Mean ($\times 10^{-9}$)	SD ($\times 10^{-9}$)	CV (%)
Left	oxy	15.1	4.4	29.2
	red	11.8	2.2	18.2
	tot	10.3	1.9	18.4
Right	oxy	13.6	4.5	32.9
	red	9.4	1.5	16.5
	tot	7.9	1.9	23.4

Modeling of the hemodynamic response. The spatially averaged Hb response curves shown in Sec. III B 2 "Spatially averaged time response of Hb signals" were used to empirically derive approximations, or models, of the hemodynamic response to stimulation for each of the oxygenation states. To establish the Hb_{oxy} model, signal intervals comprising 20 time points before and 20 time points after each response peak (6 epochs $\times$ 4 paws=24 peaks) were averaged, and a Gaussian fit to the resulting curve was chosen as the model for the Hb_{oxy} response to stimulation. Likewise, a Gaussian fit to the averaged Hb_{red} response was established as the Hb_{red} model. The reactions to all stimulation sites were averaged in order to maximize SNR and to achieve the most general response representation. To determine whether this approach is justified, we investigated the signals for different stimulation sites and found that they all are highly correlated ($r>0.9$). The averaged Hb_{oxy} and Hb_{red} response curves and their respective model functions are plotted in Fig. 9. The measured responses were subjected to linear detrending and offset correction to establish zero baselines; error bars in the graph indicate standard deviations for the experimental data. Both graphs show concentration changes in the same arbitrary units that are inherent in the MBL method.[13] It can be seen that the measured responses are well approximated by the Gaussian fits. Consistent with the observation made in Sec. III B 2 "Spatially averaged time response of Hb signals," the Hb_{oxy} model peaks about 0.5 s earlier than the Hb_{red} model does. The Gaussian fit to the Hb_{oxy} signal also is of higher magnitude (8.5 versus 7.4) and a factor of 1.4 narrower than that to the Hb_{red} curve.

The Hb_{tot} signal is not measured independently, and it shows a more complex shape and lower SNR than the Hb_{oxy} and Hb_{red} signals. We therefore did not use a curve fitting procedure to establish a Hb_{tot} response model, but instead used the sum of the Hb_{oxy} and Hb_{red} model functions. Both the measured Hb_{tot} response (averaged over all stimuli) and the calculated model are shown in Fig. 9. It can be seen that

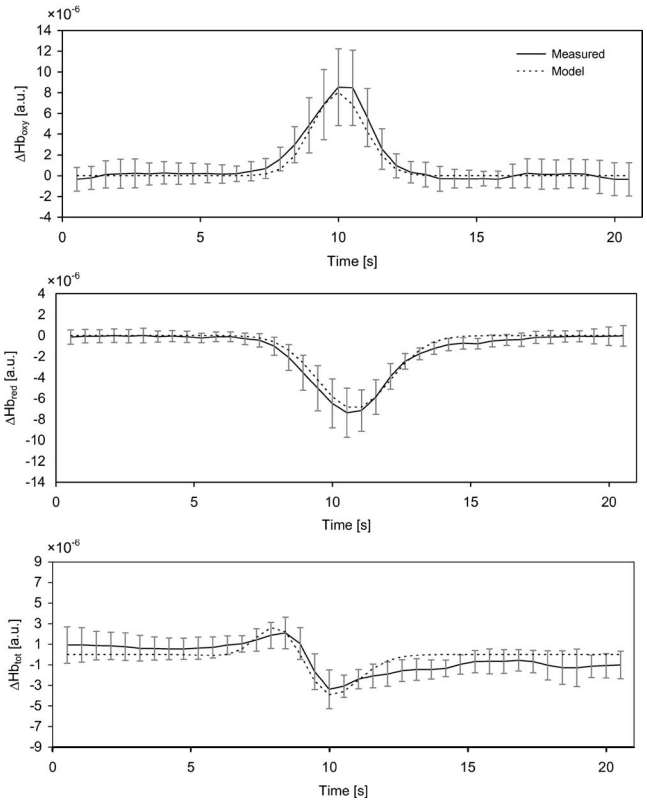

FIG. 9. Spatially integrated hemodynamic response of the rat brain to stimulation. Continuous curves represent the measured response averaged over all trials (error bars indicate standard deviation at each time point). Dashed curves are the analytically derived best-fitting functions that were used as models in the GLM calculations.

the sum of the Hb_{oxy} and Hb_{red} model functions approximates the Hb_{tot} response reasonably well. It deserves emphasis that this result was obtained without any scaling or shifting of the added functions.

GLM analysis of image time series. The reconstructed image time series were divided into four intervals corresponding to the different paw stimulation periods. For each paw and each Hb form, six model functions of equal length were constructed, each representing the idealized hemodynamic response in one stimulation epoch. Thus each of these curves was designed by centering one of the analytical shapes derived in Sec. III B 2 "Modeling of the hemodynamic response" at the time of peak stimulation response and padding it with zeros to obtain the appropriate signal length, which was about 1700 time points (15 min). GLM analysis was subsequently applied to data from each stimulation period and for each Hb form separately, using the appropriate synthesized tissue response curves as model functions. This step yields the spatial distributions of the hemodynamic response magnitude for each stimulus, as represented by the GLM coefficient at each image location. Spatial maps of the mean, standard variation, and CV of the GLM coefficients for all Hb states were created from these data sets (i.e., no data averaging was performed prior to the GLM computation). The possibility of analyzing individual stimulus responses is a consequence of the data quality achievable with the large dynamic measurement range of the imager. The six GLM results obtained for each Hb form and each paw were treated as outcomes of individual measurements, allowing statistical analysis of variations in the response patterns and of their dependence on the stimulation site.

The GLM value is a measure of the amplitude at which the model function is present in the analyzed times series; this quantity is therefore sensitive to the overall strength of the signal and does not consider the relative magnitude of the "model behavior" compared to other signal components (i.e., trends, noise, or other physiologic signals). For example, a strong GLM coefficient can be the result of a weak signal that closely follows the model function; however, it can also stem from a signal that varies strongly in absolute terms but contains a small fraction of the model signature.

This ambiguity is resolved by computing the percentage of variance accounted (PVA) for by the model function, a relative measure ranging from 0% (no presence of model) to 100% (pure model signal). Like the GLM coefficients, the PVA values were computed for each epoch separately, to enable statistical evaluation.

(1). **Differential Hb_{oxy} and Hb_{red} response**. The prototypical hemodynamic response to neuroactivation is characterized by an increase in Hb_{oxy} and a decrease in Hb_{red}, as reflected by our model functions. Areas showing this response are therefore expected to yield positive GLM coefficient values for both Hb states. To isolate occurrences of this behavior, volume-rendered maps of the rat head were created in which areas corresponding to the occurrence of positive and negative values in the mean-GLM maps for Hb_{oxy} and Hb_{red} were color encoded. Figure 10 shows the results for

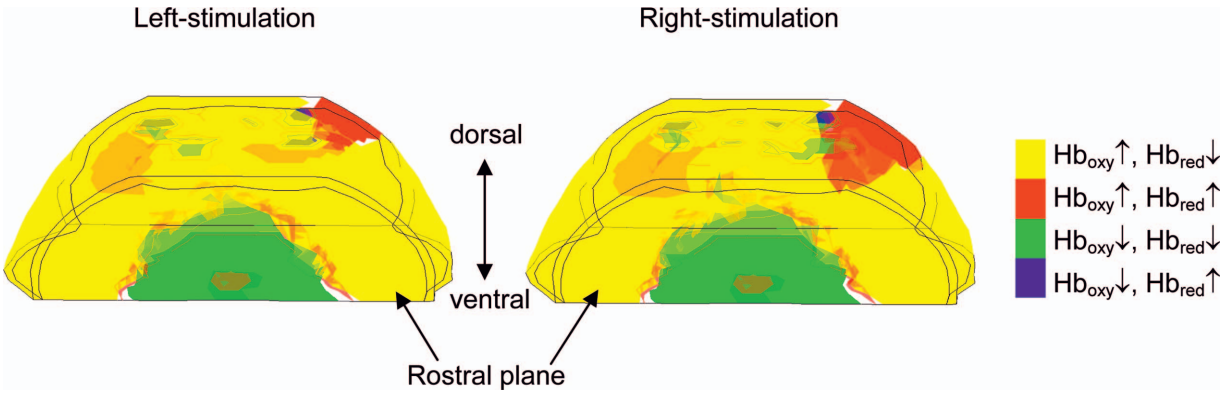

FIG. 10. (Color) Volume rendering of differential Hb_{oxy} and Hb_{red} response, color coded according to the algebraic signs of each pixels's GLM coefficients.

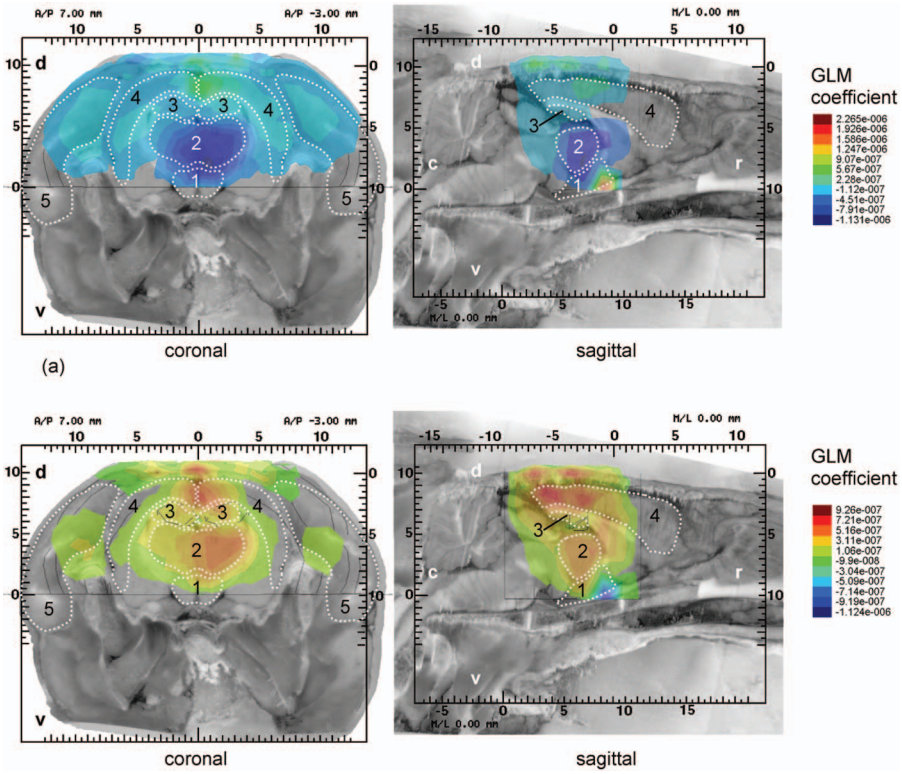

FIG. 11. (Color) Overlay of GLM results onto anatomical cross sections of the rat head for Hb_{oxy} (a) and Hb_{red} (b); *d*-dorsal, *v*-ventral, *c*-caudal, *r*-rostral, l-hypothalamus, 2–thalamus, 3–hippocampus, 4–neocortex, 5–muscles (cryosectional images, © UCLA Laboratory of Neuro Imaging, Ref. 31).

both forepaws. It can be seen that for both cases the majority of the imaged volume (>80%, yellow) shows the typical hemodynamic response with an increase in Hb_{oxy} and a decrease in Hb_{red}. This behavior is found in the general vicinity of the cortical regions and the temporalis muscles. However, a region located ventrally on the midline, in the rostral half, shows an inverted Hb_{oxy} and a regular Hb_{red} response. This behavior, rendered green, occupies about 9% of the total imaged volume. About the same fraction (8%, red) shows the opposite behavior of a regular Hb_{oxy} and an inverted Hb_{red} response. This latter reaction is seen primarily in superficial areas of the image. A negligible portion of the image ($\sim$1%) exhibits inversion in both Hb states.

(2). **GLM imaging results**. Figure 11 shows cross-sectional maps of the GLM coefficients for Hb_{oxy} [Figs. 11(a)] and Hb_{red} [Figs. 11(b)], for left forepaw stimulation, overlaid onto anatomical maps of the rat head. Depicted for both Hb states is the average of the GLM results obtained from the six stimulation epochs. The anatomical cross-sections are digitally imaged cryosections of male Sprague-Dawley rats, generated at the UCLA Laboratory of Neuro Imaging (LONI) and available from that group's website.[31] The images are part of the same rat brain atlas on which the FEM meshes were modeled (see Fig. 6). As needed, scaling and shifting operations were used to superimpose the DOT images on the anatomical images, using landmarks such as the positions of skull sutures and the hypothalamus.

The coronal section shown in Fig. 11(a) is located roughly in the center of the thalamus. Positive response maxima are seen in the neocortical compartment, in the region of the temporalis muscles, and in the dorsal scalp. The strongest cortical response appears centrally on the midline. As one would expect, regions occupied by skull bones show a generally weak functional response. A strong inverted response (i.e., negative GLM values, dark blue) is observed in the thalamus and hypothalamus. It is worth noting that the spatial distribution of the GLM results coincides well with the anatomical structures even though a homogeneous tissue model, with no spatial constraints imposed, was used for the reconstruction.

The sagittal view in Fig. 11(a), located on the midline, reveals again a strong positive response in the dorsal cortex as well as a strong inverted response in the thalamic and hypothalamic regions. A few superficial maxima are seen in the scalp layer. Most prominent in the sagittal view is the appearance of a hotspot on the ventral rendering boundary anterior to and ventral to the thalamus.

The coronal section in Fig. 11(b) indicates that maximum Hb_{red} GLM response occurs in neocortical areas close to the midline, the thalamus/hypothalamus region, and the muscles. In addition, some hot spots are seen in the scalp. Compared to the Hb_{oxy} results, the neocortical activity appears more focused on the midline with less lateral extent.

The sagittal view in Fig. 11(b) suggests that stimulation induces a strong decrease in Hb_{red} in isolated scalp areas and the dorsal neocortex, as well as in the thalamic and hypothalamic areas. A hotspot anterior and ventral to the thalamus shows an inverted response.

As discussed above, the information provided by GLM coefficients is ambiguous, in that the value depends both on the relative contribution of the modeled component to the time series and on the overall absolute signal strength. This ambiguity is resolved by PVA maps that identify the relative contribution of the hemodynamic model function to local tissue behavior. Figure 12 depicts volume renderings of the PVA results for left forepaw stimulation. Shown for each Hb

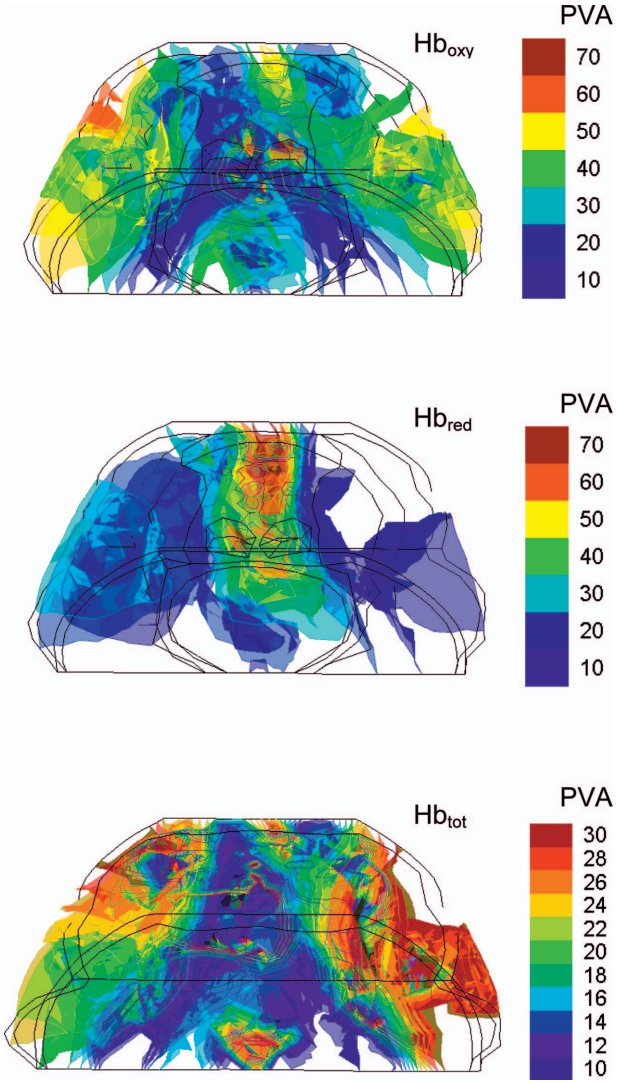

FIG. 12. (Color) Volume PVA data, obtained from GLM computations.

state is the mean PVA value, obtained by averaging the PVA results for six successive stimulation epochs. As can be seen in Fig. 12, high-PVA Hb_{oxy} responses to stimulation are found laterally in the muscle regions and centrally in the neocortex. The thalamic area also shows a fairly high model component. Incidentally, the area anterior and ventral to the thalamus that showed the largest GLM response is not prominent in the PVA result. This combination of findings is indicative of large overall signal strength with a relatively small fraction representing the model hemodynamics; this condition could result from the strong vascularization of the roof of the mouth, or from the proximity of ventral cerebral arteries. The Hb_{red} result Fig. 12 follows the model most strongly in a region confined to the cortex, about the midline. The relative response strength in muscles and thalamus appears much weaker here than in the Hb_{oxy} PVA map. The Hb_{tot} result in Fig. 12 has a response distribution qualitatively similar to that of the Hb_{oxy} image, but with about half the magnitude.

(3). **Reproducibility of GLM results**. Because GLM analysis is performed for individual stimulations, six outcomes are obtained at each image location. From these, the

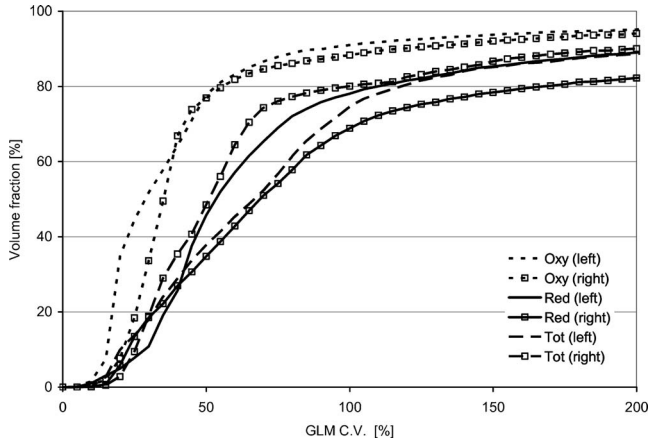

FIG. 13. Cumulative distribution functions of CV values for the image GLM coefficients.

CV can be calculated as a measure of repeatability or precision of the measurement. Figure 13 depicts the cumulative distribution functions of CV values for the image GLM coefficients. The graph indicates the fraction of reconstructed image volume having GLM repeatability at least as good as each CV value plotted on the abscissa. A steep slope indicates that the GLM coefficient precision for the majority of image elements falls within a narrow interval, whereas a flatter curve suggests a more inhomogeneous behavior, i.e., the occurrence of a wide range of GLM variabilities. The more left shifted the curve appears, the higher the overall GLM repeatability. The presented graphs indicate that the measured Hb_{oxy} reactivity occurs more homogeneously and has generally better repeatability than the results for Hb_{red} and Hb_{tot}. Table II illustrates these findings for two exemplary CV values of 50% and 80% GLM coefficient variability. It is seen that for all cases more than one third of the volume exhibits variability less than 50%, and at least three fifths of the image shows less than 80% CV between stimuli. There is no marked difference between results for left- and right-side stimulation. In both cases the Hb_{oxy} signals show significantly higher reproducibility than Hb_{red} or Hb_{tot}, which have comparable variability.

The same cumulative sum analysis was performed on the CV values for the PVA calculations. The results, summarized in Table III, are qualitatively similar to those obtained for the GLM coefficients. Again, no marked sidedness is observed. The measured Hb_{oxy} hemodynamics are systematically more repeatable than are the Hb_{red} or Hb_{tot} results, and the latter

TABLE II. GLM coefficient reproducibility.

		% of image volume	
Side	Hb state	CV≤50%	CV≤80%
Left	oxy	78	89
	red	46	72
	tot	38	61
Right	oxy	77	86
	red	35	58
	tot	48	77

TABLE III. PVA reproducibility.

		% of image volume	
Side	Hb state	CV⩽50%	CV⩽80%
Left	oxy	71	88
	red	18	56
	tot	31	72
Right	oxy	61	84
	red	21	42
	tot	23	74

show very similar characteristics to each other. Incidentally, the volumetric precision analysis also yields quantitatively similar results for both GLM and PVA values. Comparing Tables II and III, one observes very good agreement between the Hb_{oxy} reproducibility in both cases, mostly deviating by a few percent. Differences for the other Hb states are larger, but they are still within 25% for most cases.

(4). **Response lateralization**. To obtain a quantitative assessment of response lateralization, we identified areas of statistically significant differences between the GLM maps corresponding to stimulation of the left and right forepaws. A Kruskal-Wallis analysis of variance (ANOVA) test was used to compute, for each pixel, the p value between the sets of GLM coefficients obtained for each stimulation site. Here, p values $\leqslant 0.05$ are regarded as statistically significant.

The p-value computation reveals the presence of differential activation, but it does not distinguish functional behaviors. Six qualitatively different classes of hemodynamic changes, depending on the algebraic signs and the relative magnitude of the mean GLM values for left- and right-side stimulation, have been identified. They are: positive GLM coefficients for both sides, with a stronger response to left $(1, P-p)$ or to right $(2, p-P)$ forepaw stimulation; positive left-paw and negative right-paw GLM values $(3, p-n)$; negative left-paw and positive right-paw GLM coefficients $(4, n-p)$; and negative GLM values for both sides, with a stronger response to left $(5, N-n)$ or to right $(6, n-N)$ forepaw stimulation. (The shorthand notation introduced in the preceding sentence will be used throughout the remainder of this section). Each of these cases represents a specific hemodynamic reaction to a change in the stimulation side, e.g., a change from a strong Hb_{oxy} increase to a weak Hb_{oxy} increase $(P-p)$, or to a Hb_{oxy} decrease $(p-n)$. These functional distinctions can be used to detect somatosensory activation, which would be expected to cause opposing behavior in the involved areas in both hemispheres. For example, an occurrence of $p-P$ on one side of the neocortex should be matched by an area of $P-p$ behavior on the other side. Volume-rendered images of these different functional behaviors for all three Hb states are shown in Fig. 14.

For the Hb_{oxy} signal, a concentration increase (i.e., positive GLM coefficients) is noted in most areas of the tissue volume imaged, with the left-paw response being stronger than the right-paw response (P-p, light red). Regions showing flips from a positive to a negative response going from left- to right-paw stimulation ($p-n$, yellow) and vice versa

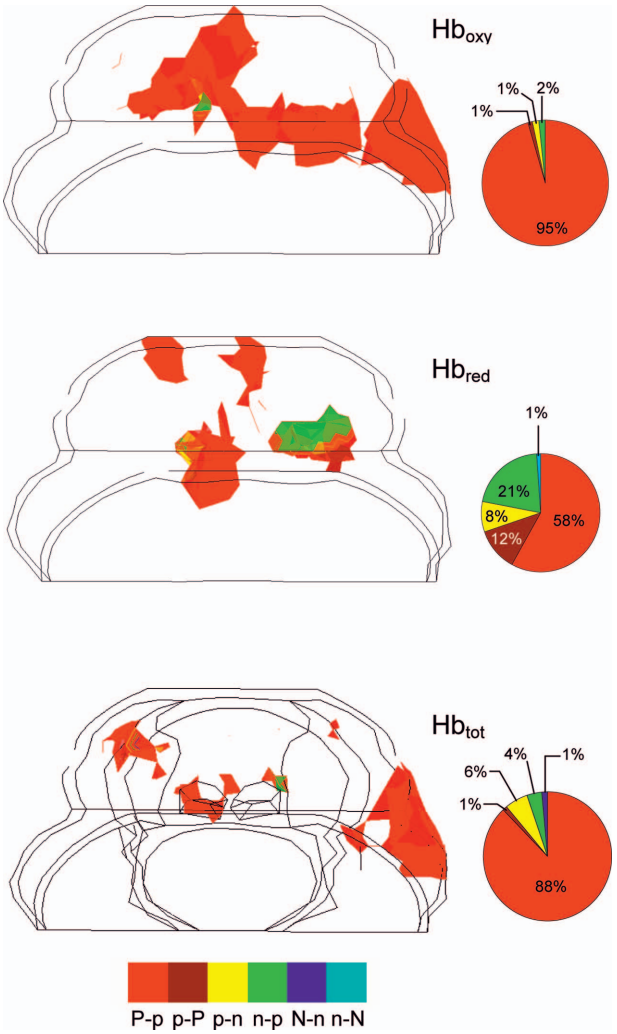

FIG. 14. (Color) Volume rendered display of areas having significantly different hemodynamic response to left and right stimulation. Different classes of reaction are color coded.

$(n-p$, green) also are observed. These latter behaviors, however, occur in only an insignificant amount of the image; they make up a combined fraction of about 3% of the total rendered volume. Differential left-vs.-right activation is observed in dorsal cortical regions and in one isolated region on the animal's left side. While most of the differential response is found in the cortex, the observed pattern is not supportive of predominant lateralized activation of the somatosensory regions, which would cause a left-right symmetric pattern with opposing behavior in both hemispheres.

In comparison, the Hb_{red} response shows a more heterogeneous distribution of different functional behaviors. The majority (70%) of significant changes stem from a positive response (i.e., Hb_{red} decrease) for both stimulation sides, however, this is the sum of 58% having a stronger reaction to left paw stimulation ($P-p$, light red), and 12% that show larger activation for the right paw ($p-P$, dark red). Also, significant amounts of flipped responses are present, with 21% of the differences being due to a change from an Hb_{red} increase to an decrease upon switching from left- to right-side stimulation, and 8% showing the opposite behavior [$n-p$ (green) and $p-n$ (yellow), respectively]. A very small

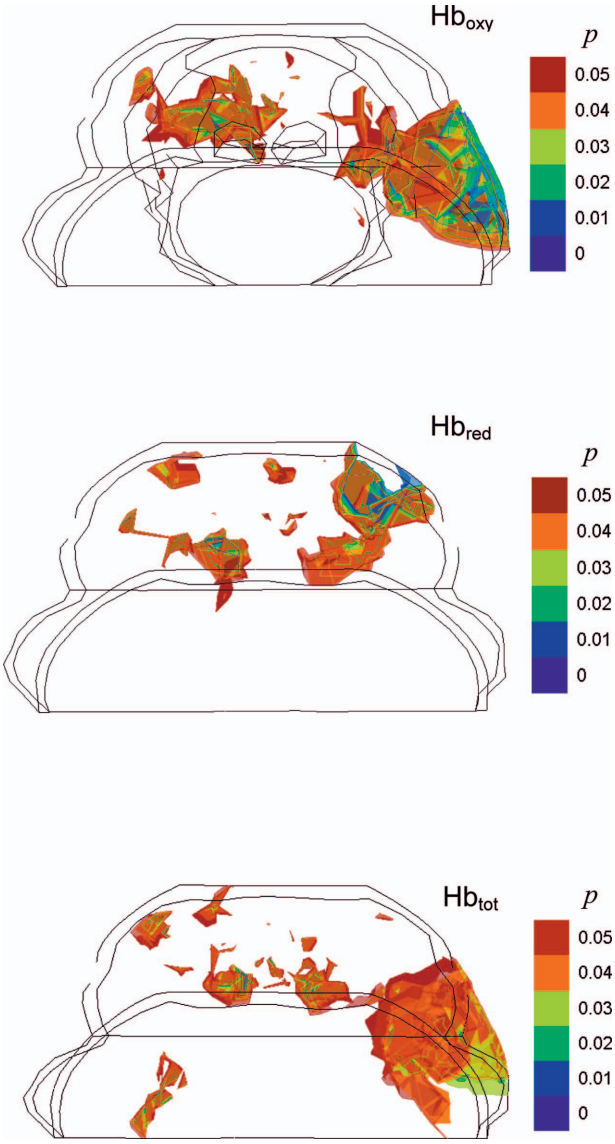

FIG. 15. (Color) Volume rendering of those head areas that show significant ($p<0.05$) differences between PVA values for stimulation of the left and right forepaws.

amount (2.5%) of inverted response for both stimulation sides is observed, with a larger magnitude for the left response. As in the Hb_{oxy} case, the result lacks the prominent left-right symmetry that one would expect from a primarily somatosensory response.

The statistical map for Hb_{tot} in Fig. 14 shows significant left versus right differences in the left cheek of the animal, similar to the Hb_{oxy} result, as well as in some smaller cortical regions. Overwhelmingly (88%), those differences are accounted for by positive GLM responses to both stimulation sides, with left-paw stimulation causing a stronger activation ($P-p$). Flipped responses show a combined 10% contribution, while other functional behaviors account for 1% or less of the functional differences. As was seen in the results for the other two Hb states, no predominant lateral response symmetry is readily apparent.

Using Kruskal-Wallis ANOVA, the PVA results were investigated further, to identify possible occurrences of response lateralization. Figure 15 depicts, for each Hb state,

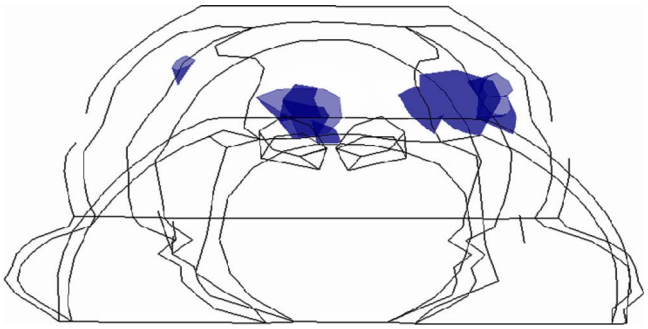

FIG. 16. Volume rendering of those brain regions which react in a significantly different manner to stimulation of left and right forepaws, for both Hb_{oxy} and Hb_{red}.

those areas exhibiting a significant difference between PVA values for left-forepaw and right-forepaw stimulation. For all Hb states, clusters of differential response are distributed throughout the cortical areas. In addition, the Hb_{oxy} and Hb_{tot} images show significant response differentiation in the animal's left cheek. The results do not reveal a clearly lateralized reaction to paw stimulation, but rather suggest globally distributed responses. To extract possible lateralized somatosensory activation, those regions were identified that show significant asymmetric reactions for both Hb_{oxy} and Hb_{red} PVA results. Fig. 16 is a representation of these areas, which were obtained as the intersection of the Hb_{oxy} map and the Hb_{red} map in 15. Two distinct areas of the neocortex, roughly symmetric across the midline, are visible, suggesting the presence of a somatosensory component in the hemodynamic signal.

IV. DISCUSSION

A. Technology innovations

The small-animal DOT imaging system described here was based on a published instrumentation design[13,17] that has proved applicable to a range of human imaging applications. Important features of the new instrument are four-wavelength illumination and inclusion of a MRI-compatible small-animal imaging platform. The first of these innovations permits more accurate quantification of hemoglobin changes than is possible with earlier two-wavelength systems,[13] and also can enable users to compute estimates of concentrations for other tissue chromophores; the latter provides stereotaxic animal fixation and achieves stable fiber contact for a wide range of possible probe arrangements. Quality control tests performed with laboratory phantoms, and preliminary experimental animal data, demonstrate that the modified system continues to meet the fundamental performance criteria that have guided our instrumentation development effort all along.[17] These include: the ability to collect complete sets of tomographic data at rates greater than 1 Hz, high SNR, low short- and long-term instrument drift, and a large dynamic range with linear instrument response over the full range. Owing to the speed, noise, and stability properties, the system is suitable for dynamic measurements of hemodynamic responses to physiological provocations, or of naturally occurring hemodynamic fluctuations. The large dynamic range allows for use of S/D configurations that are fully tomogra-

phic (or as near to it as permitted by anatomical constraints).

The preceding consideration was the reason for adopting the S/D geometry described above, which combines a large number of cranial optodes with a small number placed at more distant sites (i.e., ears and mouth). Numerical simulations we have conducted (results not shown) confirm that, relative to a pure back-reflection optode arrangement,[9,10] addition of a few array-opposing optodes improves sensitivity to deep-lying structures, and image accuracy. This finding is in agreement with a numerical simulation study by Xu *et al.* that compared image quality for a one-sided fiber array opposed by a single probe with a probe arrangement that fully encircled the imaged volume,[32] and found comparable image quality for the two measurement geometries.

B. Physiological findings

As revealed by the image postprocessing steps described above, the dominant effect of the paw stimulations was a global hemodynamic response that was not strongly lateralized. The spatial pattern seen is suggestive of activation of pain pathways, which are known to involve multiple areas of the neocortex as well as thalamus and hypothalamus.[33,34] Our use of higher electric stimulation current than reported in other studies with a similar protocol[28] lends further plausibility to the pain-pathway activation hypothesis.

An integral part of the global reaction to stimulation is the inverted Hb_{oxy} response in the thalamus/hypothalamus region. The observed decrease in Hb_{tot} (i.e., both Hb_{oxy} and Hb_{red} fall in response to stimulation) is contrary to the stereotypical hemodynamic reaction. Also unexpected was the strong hemodynamic response in the muscle regions. The former result is suggestive of a vascular shunting phenomenon, and the latter may indicate a reflex reaction to the electric stimulation; only speculative interpretations are possible at this time, however, given the small quantity of experimental data at hand.

While the apparent recovery of a lateralized somatosensory response also is speculative, we find the final result presented above encouraging because the regions identified (again, without incorporating *a priori* information into the image postprocessing computations) closely approximate the portions of the brain where neuronal activation would be expected, and because of the plausibility of each of the computational steps. Thus we fully expect that lateralized hemodynamic responses will be seen more readily in future experiments that will be more carefully conducted with regard to stimulus current and other control variables.

Results of the systems checks and the preliminary animal experiment lead us to conclude that the dynamic imaging system described here is suitable for use as a monitor of hemodynamic changes in long-term animal behavior studies. It seems clear that the constellation of instrumentational (i.e., speed, stability, SNR, dynamic range[13,17]) and computational (e.g., image reconstruction algorithms that are fast and robust to noise and to known forms of experimental uncertainties[23–25]) features possessed by the system presented here would be required of any device intended to be used for experiments of that type.

C. Future considerations

The primary goal of the rat-brain study presented here was to test our instrumentation and analysis approach to functional optical small-animal imaging. As indicated in the preceding section, a major goal for future experiments will be to conduct behavioral studies on freely moving animals, similar to those that have previously been conducted using electrical recordings as the means of monitoring cerebral activity.[35,36] Accordingly, wearable measuring heads that will permit simultaneous optical and electrical recordings are currently being designed and manufactured. We also plan to conduct a more rigorous exploration of the influence of experimental control parameters on the relative magnitudes of somatosensory brain response and the activation of pain pathways evoked by the stimulation protocol employed. As already indicated, the latter activation overpowered the former in the experiment reported on here, presumably because of the magnitude of the applied electrical current. Thus, future experiments involving the same basic protocol will explore gradations in stimulation parameters (e.g., current, pulse length, repetition rate), with the objective of reducing the extent of pain-pathway activation and minimizing the ratio of the latter to the somatosensory response.[37]

ACKNOWLEDGMENTS

The authors wish to thank Dr. Avraham Y. Bluestone and Dr. Andreas H. Hielscher, for providing the anatomical atlas-based geometry used for the reported inverse problem computations, and for many helpful conversations. This research was supported in part by the National Institutes of Health (NIH) under Grant Nos. R21-HL67387, R21-DK63692, R41-NS50007, R43-NS49734, and R43-HL77059.

[1] R. Weissleder and U. Mahmood, Radiology **219**, 316 (2001).
[2] E. E. Graves, J. Ripoll, R. Weissleder, and V. Ntziachristos, Med. Phys. **30**, 901 (2003).
[3] A. D. Klose and A. H. Hielscher, Opt. Lett. **28**, 1019 (2003).
[4] A. Grinvald, E. Lieke, R. D. Frostig, C. D. Gilbert, and T. N. Wiesel, Nature (London) **324**, 361 (1986).
[5] A. Villringer and B. Chance, Trends Neurosci. **20**, 435 (1997).
[6] J. Mayhew, D. Hu, Y. Zheng, S. Askew, Y. Hou, J. Berwick, P. J. Coffey, and N. Brown, Neuroimage **7**, 49 (1998).
[7] D. B. Polley, E. Kvašňák, and R. D. Frostig, Nature (London) **429**, 67 (2004).
[8] J. P. Culver, T. Durduran, D. Furuya, C. Cheung, J. H. Greenberg, and A. G. Yodh, J. Cereb. Blood Flow Metab. **23**, 911 (2003).
[9] A. Y. Bluestone, M. Stewart, J. M. Lasker, G. S. Abdoulaev, and H. Hielscher, J. Biomed. Opt. **9**, 1046 (2004).
[10] A. Y. Bluestone, M. Stewart, B. Lei, I. S. Kass, J. M. Lasker, G. S. Abdoulaev, and A. H. Hielscher, J. Biomed. Opt. **9**, 1063 (2004).
[11] A. M. Siegel, J. J. A. Marota, and D. A. Boas, Opt. Express **4**, 287 (1999).
[12] B. W. Pogue, T. O. McBride, C. Nwaigwe, U. L. Oesterberg, J. F. Dunn, and K. D. Paulsen, Proc. SPIE **3597**, 484 (1999).
[13] C. H. Schmitz *et al.*, Appl. Opt. **44**, 2140 (2005).
[14] N. A. Franco *et al.*, Presented at the 4th Optical Imaging Workshop at the NIH Bethesda, MD, September 20–22, 2004.
[15] D. P. Klemer *et al.*, Proceedings OSA Biomedical Optics Topical Meetings, Advances in Optical Imaging and Photon Migration, Miami Beach, FL, April 14–17, 2004.
[16] D. Piao, S. Jiang, S. Srinivasan, P. K. Yalavarthy, X. Song, and B. W. Pogue, Proc. SPIE **5693**, 129 (2005).
[17] C. H. Schmitz, M. Löcker, J. Lasker, A. H. Hielscher, and R. L. Barbour, Rev. Sci. Instrum. **73**, 429 (2002).
[18] C. H. Schmitz *et al.*, Appl. Opt. **36**, 6466 (2000).
[19] C. H. Schmitz, Y. Pei, H. L. Graber, J. M. Lasker, A. H. Hielscher, and R.

L. Barbour, Proc. SPIE **4431**, 282 (2001).
[20] A. E. Cerussi, D. Jakubowski, N. Shah, F. Bevilacqua, R. Lanning, A. J. Berger, D. Hsiang, J. Butler, R. F. Holcombe, and B. J. Tromberg, J. Biomed. Opt. **7**, 60 (2002).
[21] C. Li, H. Zhao, and H. Jiang, Proceedings OSA Biomedical Optics Topical Meetings, Advances in Optical Imaging and Photon Migration, Miami Beach, FL, April 14–17, 2004.
[22] T. O. Mcbride, B. W. Pogue, S. Jiang, U. L. Osterberg, K. D. Paulsen, and S. P. Poplack, J. Biomed. Opt. **7**, 72 (2002).
[23] Y. Pei, H. L. Graber, and R. L. Barbour, Appl. Opt. **40**, 5755 (2001).
[24] Y. Pei, H. L. Graber, and R. L. Barbour, Proc. SPIE **4955**, 236 (2003).
[25] Y. Pei, H. L. Graber, Y. Xu, and R. L. Barbour, Proceedings OSA Biomedical Optics Topical Meetings, Advances in Optical Imaging and Photon Migration, Miami Beach, FL, April 14–17, 2004.
[26] J. Choi *et al.*, J. Biomed. Opt. **9**, 221 (2004).
[27] H. L. Graber, Y. Pei, R. L. Barbour, D. K. Johnston, Y. Zheng, and J. E. Mayhew, Proc. SPIE **4955**, 31 (2003).
[28] J. P. Culver, A. M. Siegel, J. J. Stott, and D. A. Boas, Opt. Lett. **28**, 2061 (2003).
[29] U. Lindauer, G. Royl, C. Leithner, M. Kühl, L. Gold, J. Gethmann, M. Kohl-Bareis, A. Villringer, and U. Dirnagl, Neuroimage **13**, 988 (2001).
[30] J. Berwick, C. Martin, J. Martindale, M. Jones, D. Johnston, Y. Zheng, P. Redgrave, and J. Mayhew, J. Cereb. Blood Flow Metab. **22**, 670 (2002).
[31] UCLA Laboratory of Neuro Imaging (LONI) ⟨http://www.loni.ucla.edu/Atlases/⟩.
[32] H. Xu, H. Dehghani, B. W. Pogue, R. Springett, K. D. Paulsen, and J. F. Dunn, J. Biomed. Opt. **8**, 102 (2003).
[33] R. C. Coghill, C. N. Sang, J. Ma. Maisog, and M. J. Iadarola, J. Neurophysiol. **82**, 1934 (1999).
[34] A. Ploghaus, I. Tracey, J. S. Gati, S. Clare, R. S. Menon, P. M. Matthews, and J. N. P. Rawlins, Science **284**, 1979 (1999).
[35] R. U. Muller, J. L. Kubie, and J. B. Ranck, Jr., J. Neurosci. **7**, 1935 (1987).
[36] A. A. Fenton, G. Csizmadia, and R. U. Muller, J. Gen. Physiol. **116**, 191 (2000).
[37] D. T. Raceyt, in *The Rat Nervous System*, edited by G. Paxinos (Elsevier Academic, San Diego, CA, 1978), Chap. 25.